Structural Confinement Effects of Ternary Chalcogenide in Mesoporous AlMCM-41 of Different Pore Diameters

Weon-Sik Chae and Yong-Rok Kim*

Department of Chemistry, Yonsei University, Seoul, 120-749, South Korea

Jin-Seung Jung

Department of Chemistry, Kangnung National University, Kangnung, 210-702, South Korea

Received: April 3, 2002; In Final Form: October 30, 2002

Structural confinement effects of amorphous ternary chalcogenide of $Ni_3(SbTe_3)_2$ in mesoporous channels of different pore diameters have been studied. Insertion of the guest into the channels of AlMCM-41 was probed by the results of transmission electron microscopy (TEM), nitrogen adsorption, X-ray diffraction (XRD), and photoluminescence (PL) and photoluminescence excitation (PLE). From powder XRD patterns, characteristic diffraction peaks were observed for the ternary chalcogenide incorporated in AlMCM-41, which indicated long-range ordering and increased crystallinity. The competition between the homogeneous broadening and the inhomogeneous broadening of the characteristic XRD peak profiles of the guest chalcogenides are evaluated in a series of the hosts. As the mesopore diameter decreases, the strain is enlarged in the nanosize guest chalcogenide while the estimated particle size from the full width at half-maximum (fwhm) of the respective Lorentzian profiles is similarly preserved. The characteristic energy level, for the nanophase ternary chalcogenide, induced by the strain is gradually red shifted in the nanocomposites with decreasing the pore diameter. The structural confinement causes the suppression of phonon coupling to the photoexcited carriers in the ternary chalcogenide incorporated in AlMCM-41, and the coupling is more suppressed in the nanocomposite of smaller pore diameter. Such phonon suppression induced by the structural confinement results in longer PL lifetimes as the pore diameter decreases.

Introduction

Amorphous intermetallic chalcogenide compounds have a wide variety of physical characteristics from electrical to magnetic properties, such as semiconducting property, spin-glass behavior, etc.[1] A simple metathesis reaction between divalent transition metal halides and Zintl phase precursors provides amorphous intermetallic chalcogenide compounds.[2−7] The syntheses of the amorphous intermetallic chalcogenide compounds of $M_3(SbTe_3)_2$ and $M_3(GaTe_3)_2$ (M = Cr, Mn, Fe, Co, Ni) were reported by Jung and co-workers, using Zintl phase precursors of K_3SbTe_3 and K_3GaTe_3, respectively.[8−10] Some amorphous intermetallic chalcogenide compounds show spin-glass behavior at the extremely low temperatures of 3−22 K. Under irradiation of laser, a magnetic bubble or magnetic hole is generated below the spin-glass freezing temperature.[8−10] These photomagnetic effects in amorphous intermetallic chalcogenide compounds have a potential application of high-density magnetooptic storage medium for erasable magnetic memory devices. For these amorphous intermetallic chalcogenide compounds, however, few spectroscopic studies have been reported to understand the physical characteristics induced by the restricted environments.

Recently, an amorphous ternary chalcogenide compound of $Ni_3(SbTe_3)_2$ and its nanocomposite with the mesoporous aluminosiliceous host (AlMCM-41) have newly been studied by using spectroscopic tools.[11] The host material with well-ordered hexagonal honeycomb array prohibits particle aggregation, resulting in a discrete nanophase domain in the mesoporous channel. In addition, novel physical properties have emerged from the structurally confined ternary chalcogenide in the mesoporous AlMCM-41 host. Such physical properties are due to the suppression of the phonon coupling to photoexcited carriers. The phonon suppression induces longer PL lifetimes in the nanocomposite compared with the amorphous bulk, which also causes the long-range ordering and the weak ferromagnetic coupling in the mesoporous host channel.[11] In the present study, the effects induced by different degrees of structural confinements are discussed for the ternary chalcogenide compound in the mesoporous AlMCM-41 host of different pore diameters.

Experimental Section

Synthesis. Since the mesoporous siliceous material (MCM-41) was first synthesized,[12] the porous materials with mesoscopic size (2 nm < d < 50 nm) have opened a novel phenomena in nanosize materials. In this study, the amorphous ternary chalcogenide of $Ni_3(SbTe_3)_2$ is incorporated into a series of the mesoporous hosts of different pore diameters.

Previously, $Ni_3(SbTe_3)_2$ was prepared by the rapid precipitation of nickel(II) bromide with the Zintl phase of K_3SbTe_3 as a precursor in polar solvent.[8] For the preparation of the nanophase $Ni_3(SbTe_3)_2$ incorporated in the mesoporous channel, the negatively charged aluminosilicate, AlMCM-41 (with MCM-41 structure), was used as a host. The detailed procedures to prepare the host have previously been reported in refs 13 and 14. The respective surfactant molecules with different lengths of hydrocarbon chain—hexadecyltrimethylammonium chloride (C16TMACl, 25% solution in water, Aldrich), myristyltrim-

* To whom correspondence should be addressed.

10.1021/jp020893c CCC: $25.00
Published on Web 01/23/2003

ethylammonium bromide (C14TMABr, Aldrich), and dodecyltrimethylammonium bromide (C12TMABr, Aldrich)—are dissolved in water for the formation of the respective hexagonal liquid crystal phases. These liquid crystal phases are combined with sodium silicate solution (Aldrich), sodium aluminate solution (Sigma), and ammonia solution, providing three different channel diameters of the porous hosts (C16AlMCM, C14AlMCM, and C12AlMCM are hereafter denoted, respectively, as the host pore diameter decreases) under the condition of pertinent pH adjustment and hydrothermal treatment.[15,16] The hydrocarbon surfactants that exist in the inner channel of the final white powder are removed by calcination at 813 K for 4 h in order to incorporate only the guest molecules into their well ordered one-dimensional (1-D) channels.

The resulting negatively charged aluminum-rich aluminosilicate (Si/Al = ~7) enhances the ion exchange capacity. In 0.05M nickel(II) bromide solution, Ni(II) ion substitution for the Na-(I) ion compensating negative charge of the surface of the host wall is accomplished three times through the batch process according to the previous reports.[11,13] After evacuation of water from the Ni(II) ion exchanged AlMCM-41 hosts, the addition of K_3SbTe_3 solution into the Ni(II)-AlMCM-41 hosts results, through in part capillary action, in the final gray colored powder form of the nanocomposites, the $Ni_3(SbTe_3)_2$ incorporated in AlMCM-41 hosts (hereafter we denote them as NSTC16AlM, NSTC14AlM, and NSTC12AlM, respectively, as the host pore diameter decreases). Because of the air sensitivity of the ternary chalcogenide, all chemical processes were carried out in argon gas using glovebox and conventional Schlenk line technique.

Structural Analysis. Quantitative analysis for the ternary chalcogenides loaded in a series of the mesoporous hosts was performed by an atomic absorption spectroscopy (Perkin-Elmer AA100), which resulted in the observation that the contents of the ternary chalcogenide loaded in a series of the mesoporous AlMCM-41 hosts of NSTC16AlM, NSTC14AlM, and NSTC12AlM were 6.74, 7.20, and 6.70 wt %, respectively.

Nitrogen adsorption measurements were carried out using an adsorption analyzer (Micromeritics ASAP 2010). Before the measurements were taken, the samples were degassed for 2 h at 473 K under a vacuum of $\sim 10^{-3}$ Torr. The ternary chalcogenide compounds incorporated in the various pore diameters of the AlMCM-41 hosts are of powdered type with gray color. To characterize the particle morphology and size in the mesoporous channels, powder X-ray diffraction (XRD) data in wide-angle region ($2\theta > 10$) were collected on a diffractometer (Philips X′Pert MPD) equipped with copper radiation ($\lambda = 1.5418$ Å) and a graphite monochromator. X-ray diffraction data in the small-angle region ($2\theta < 10$) were obtained on a diffractometer (Mac Science M03XHF[22]) equipped with copper radiation ($\lambda = 1.54056$ Å). To obtain the transmission electron microscopy (TEM) images, the samples were ultrasonically dispersed in acetone and a droplet of the suspension was deposited on a holey carbon copper grid. The TEM images were obtained with a transmission electron microscope (Philips CM-20) operated at 200 kV.

Spectroscopic Analysis. Steady-state photoluminescence (PL) and photoluminescence excitation (PLE) spectra were measured with a fluorimeter (Hitachi F-4500). Temperature control was accomplished by using a silicon oil circulator in the temperature range of 275−350 K, and the low-temperature experiment at 77 K was conducted in a Dewar vessel cell containing liquid nitrogen.

A picosecond time-correlated single photon counting (TC-SPC) system was employed for the time-resolved PL decay measurements. The system consisted of a cavity dumped dual-jet dye laser (Coherent 700 series) which was synchronously pumped by a Nd:YAG laser (Coherent Antares 76-YAG). The full width at half-maximum (fwhm) of the instrumental response function was 67 ps. The exponential fittings were performed by the iterative least-squares deconvolution fitting method. The PL spectra, PLE spectra, and PL lifetime measurements were performed in a same experimental condition for all powdered samples in a closed quartz cuvette filled with argon gas.

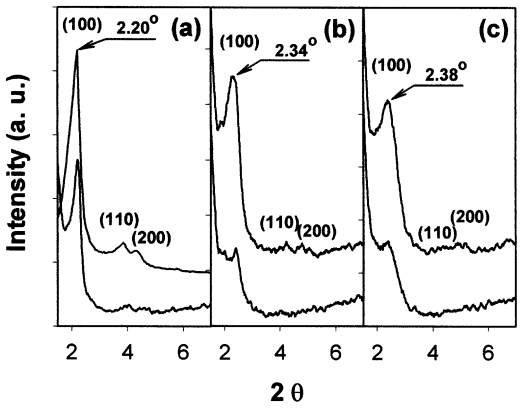

Figure 1. Powder X-ray diffractions of the hosts (upper) and the nanocomposites (lower): (a) C16AlMCM and NSTC16AlM, (b) C14AlMCM and NSTC14AlM, and (c) C12AlMCM and NSTC12AlM.

Results and Discussion

Structural Characterization. The powder XRD patterns of the hosts of different pore diameters, C16AlMCM, C14AlMCM, and C12AlMCM, exhibit characteristics of hexagonally arrayed porous structures as shown in Figure 1. The characteristic hexagonal diffraction patterns with the miller planes of (100), (110), and (200) can be assignable to the mesoporous hosts (Figure 1).

The (100) miller plane of a series of the hosts is shifted to higher angle ($2.20° < 2.34° < 2.38°$) as the sample changes from C16AlMCM to C12AlMCM, which indicates that the channel diameter of the host is gradually reduced for the following sequence of the hosts: C16AlMCM > C14AlMCM > C12AlMCM. After insertion of the guest chalcogenide, the diffraction intensity of the mesoporous host is somewhat reduced compared with that of the corresponding host before the insertion. The reduced diffraction intensity is considered to be due to the pore filling of the mesoporous host by the guest chalcogenide as suggested by the previous reports.[17,18]

Nitrogen adsorption isotherms for the mesoporous hosts exhibit the characteristic capillary condensation with type IV isotherm (Figure 2). As the length of surfactant utilized for preparation of the mesoporous host is shorter, the capillary condensation of the mesoporous host is observed in lower part of the relative pressure (P/P_0) which is indicated by arrow in Figure 2. Such lower part of P/P_0 implies reduced channel diameter of the mesoporous host. The diameter of mesoporous channel (w_d) is estimated from the following equation with primary pore volume (V_p) and d-spacing of the mesoporous host:[19−21]

$$w_d = cd\left(\frac{\rho V_p}{1+\rho V_p}\right)^{1/2} \quad (1)$$

where d is the $d_{(100)}$-spacing from XRD diffraction, ρ is the density of mesoporous wall (approximated to be ~ 2.2 g/cm^3 for the dilutely aluminum doped silica),[20,21] and c is the

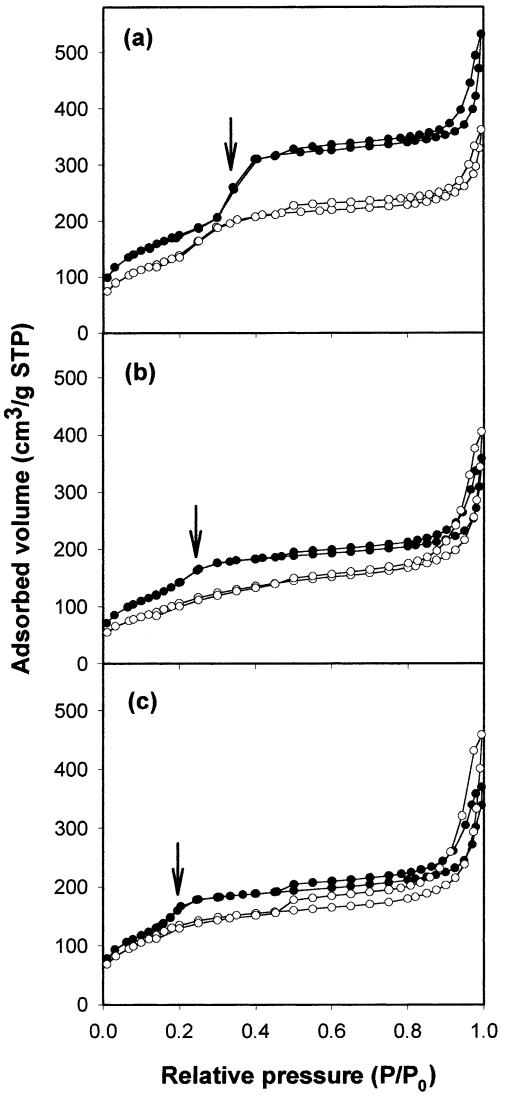

Figure 2. Nitrogen adsorption isotherms of the hosts (closed circle) and the nanocomposites (open circle): (a) C16AlMCM and NSTC16AlM, (b) C14AlMCM and NSTC14AlM, and (c) C12AlMCM and NSTC12AlM. Characteristic capillary condensations of the mesoporous hosts are marked with arrows.

geometrical constant (1.213) for circular channel.[19−21] The $d_{(100)}$ interplanar spacings and the estimated pore diameters are listed in Table 1.

After insertion of the guest chalcogenide into the C16AlMCM host, the capillary condensation is shifted to the lower part of the relative pressure with suppression of the adsorbed volume (Figure 2a). For the cases of the C14AlMCM and C12AlMCM, the characteristic capillary condensation is largely suppressed (Figure 2b, c). Furthermore, all of the mesoporous hosts exhibit reduced primary pore volume and BET surface area (S_{BET}) after the guest insertion. The detailed results of the nitrogen adsorption are shown in Table 1. From such results, it is suggested that the guest chalcogenide is located inside of the mesoporous host channels, which results in the pore filling effect in the XRD patterns.

Figure 3 shows the TEM images of the nanocomposites. The images (Figure 3a,b) present the guest incorporated nanocomposites of NSTC16AlM and NSTC14AlM and do not show bulk $Ni_3(SbTe_3)_2$ particle images existing outside of the host channels. The long-range ordered channel (Figure 3a) of the host is conserved after incorporation of the guest. Although the discrete particle images of the ternary chalcogenide in the C16AlMCM

TABLE 1: XRD $d_{(100)}$ Interplanar Spacing, BET Surface Area (S_{BET}), Primary Pore Volume (V_p), and Channel Diameter (w_d) of the Respective Hosts before and after the Guest Insertion

sample	$d_{(100)}$-space (nm)	S_{BET} (m^2/g)	V_p (cm^3/g)[a]	w_d (nm)
C16AlMCM	4.01	636.2	0.56	3.62
NSTC16AlM	3.99	510.1	0.39	3.30
C14AlMCM	3.82	534.5	0.37	3.11
NSTC14AlM	*b*	399.6	0.27	*b*
C12AlMCM	3.71	610.7	0.40	3.07
NSTC12AlM	*b*	518.8	0.19	*b*

[a] Primary pore volume is estimated from the total pore volume after subtracting the macropore volume that is approximated to the adsorbed volume in the relative pressure range above 0.7. [b] Because the interplanar spacings ($d_{(100)}$) and the channel diameters (w_d) of the NSTC14AlM and the NSTC12AlM are difficult to be exactly estimated because of the much suppressed diffraction intensities after the guest insertion, these values are not provided.

channels are not resolved from the contrast of channels and wall frameworks, the nanocomposite presents overall dark colored image (Figure 3a). For the NSTC14AlM, it is noticeable that the outer dark region of the host (indicated by arrow in Figure 3b) is presented. This dark colored image is believed to indicate the heavy atomic guest molecules of the ternary chalcogenides existing in the outer region of the host channels. The similar imaging effect has also been reported in the case of Pt clusters impregnated in mesoporous AlMCM-41.[14] Therefore, the TEM image implies that the incorporation of the guest molecules into the host channels is sterically hindered from inserting into the more inner part of the C14AlMCM channels because of the smaller channel diameter than that of the C16AlMCM. For the NSTC12AlM, although the long-range ordered pattern of the mesoporous channels is not clearly shown contrary to the cases of NSTC16AlM and NSTC14AlM, the porous structure (as proved in XRD pattern) can still be observable (inset of Figure 3c). The detailed characteristics of the incorporated guest in C12AlMCM as well as C14AlMCM and C16AlMCM is discussed, based on the results of PL and PL lifetime studies, in the later section.

For a series of the specimens, Figure 4a exhibits a weak diffraction peak at 31.5° of 2θ for the NSTC16AlM, whereas both the host (AlMCM-41) (Figure 4d) and the amorphous bulk ($Ni_3(SbTe_3)_2$) show no apparent diffraction peak in the same region of the angle.[8] Furthermore, it is noticeable that the diffraction peak is gradually broadened as the channel diameter of the mesoporous hosts decreases.

In general, the Bragg peak broadening of nanoparticles is caused by both the small particle size and the atomic level distortion (strain). A quick approximation of the size and the strain broadening can be obtained from the fwhm of a Bragg peak.[22] The observed diffraction peak profile ($2\theta = 31.5°$) in this study are reasonably well fitted, as shown in Figure 5, by a convolution of Lorentzian and Gaussian functions which are related to the homogeneous size broadening and the strain broadening components, respectively.[22] Table 2 shows the respective fwhm values for the fitted Lorentzian and Gaussian functions of the nanocomposites of the different pore diameters. As shown in Table 2, the fwhm value of the Gaussian profile shows a gradual increase with decreasing the pore diameter. Moreover, as the mesoporous channel diameter becomes smaller, the amplitude of the respective Gaussian profile (dotted line) also gradually increases compared with that of the respective Lorentzian profile (dashed line) (Figure 5). It implies that the strain of the nanocomposites is enlarged in the host of smaller pore diameter. Previously, it has been reported that the small

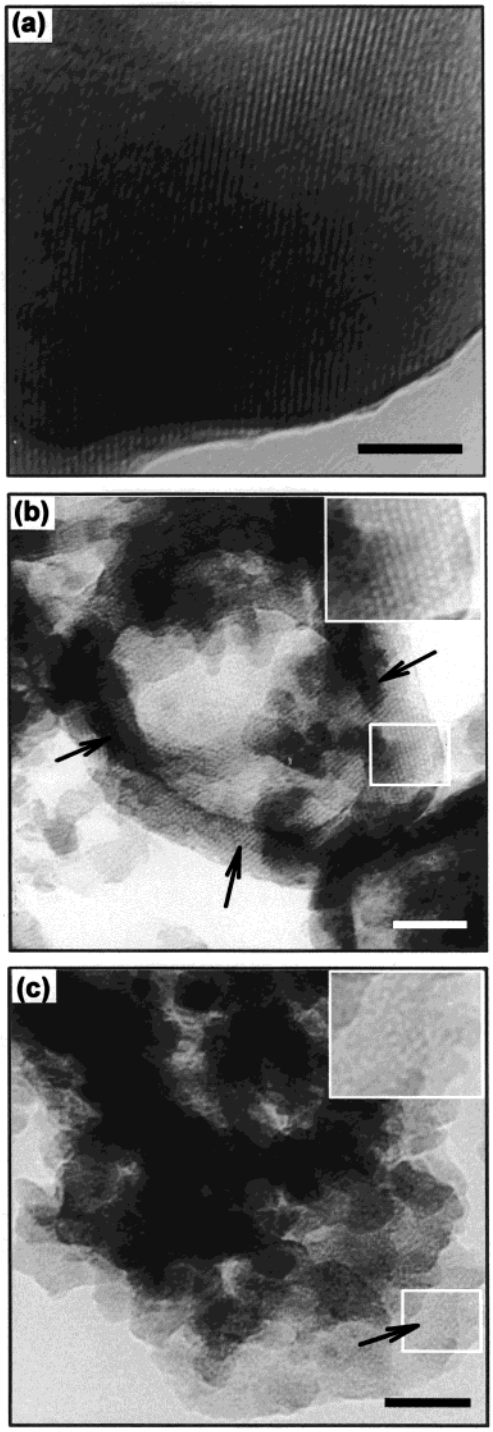

Figure 3. TEM images at a perpendicular direction to the pore opening (lamellar) for (a) NSTC16AlM nanocomposites, (b) NSTC14AlM, and (c) NSTC12AlM. Magnified images in the selected areas of NSTC14AlM and NSTC12AlM are presented in the insets of the corresponding figures. The reference scale bar is 50 nm.

clusters of nanometer size can experience a lattice contraction by the static pressure of mesoporous zeolite host.[23] In our XRD patterns, however, any discernible shift of the diffraction peaks due to the lattice contraction is not perceived, but the broadening of the diffraction peaks is observed. Therefore, it is believed that the strong coupling between the guest and the mesoporous host channel causes a lattice strain of the guest, which results in a disordered lattice structure (partial armorphization) in the guest without the lattice contraction as the pore diameter decreases.

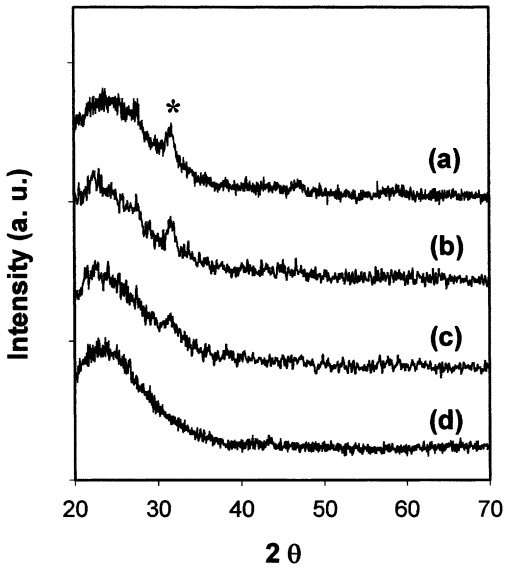

Figure 4. Powder X-ray diffractions of the nanocomposites: (a) NSTC16AlM, (b) NSTC14AlM, (c) NSTC12AlM, and (d) AlMCM-41 host. Asterisk indicates the newly emerged diffraction peak for the NSTC16AlM. The powder X-ray diffraction of NSTC16AlM is quoted from the previous study.[11]

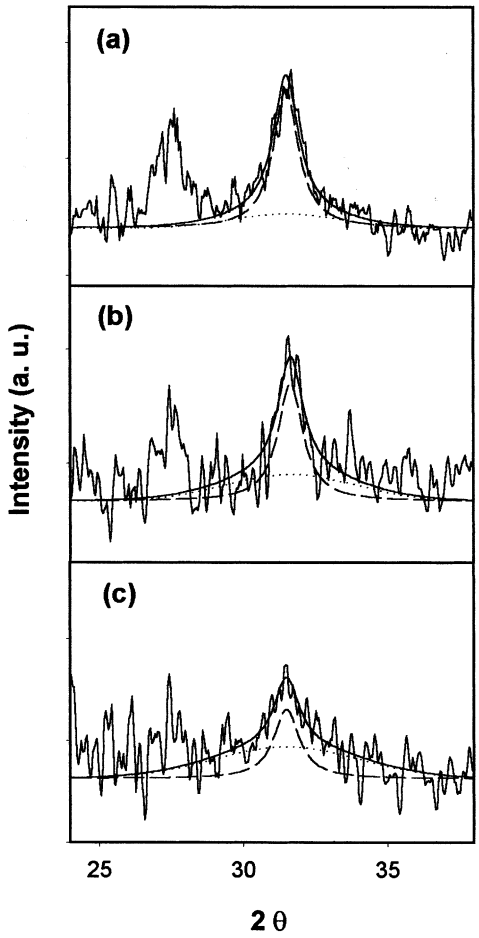

Figure 5. Convolution fitting of Lorentzian (dashed line) and Gaussian (dotted line) functions for the diffraction peak of 31.5° of 2θ: (a) NSTC16AlM, (b) NSTC14AlM, and (c) NSTC12AlM. The diffraction patterns are presented after the background subtraction corresponding to the broad diffraction of the amorphous wall framework of the host.

From the Bragg peak broadening, the average particle size of the guest incorporated in the mesoporous channels can be

TABLE 2: Estimated Particle Sizes by Scherrer Equation from the Bragg Peak Broadening

$Ni_3(SbTe_3)_2$ in hosts	fwhm (2θ) of Lorenzian's	fwhm (2θ) of Gaussian's	cluster size (nm)[a]
NSTC16AlM	1.05° (± 0.10°)	3.80° (± 0.30°)	7.9 (± 0.7)
NSTC14AlM	1.06° (± 0.12°)	4.50° (± 0.30°)	7.8 (± 0.8)
NSTC12AlM	1.08° (± 0.15°)	5.10° (± 0.40°)	7.7 (± 0.9)

[a] The clusters size is estimated from the fwhm of Lorentzian profile of the respective nanocomposites.

deduced by the Scherrer equation from the respective Lorentzian profiles without including the strain factor which corresponds to the Gaussian profiles (Table 2).[22] Because the amorphous guest existing outside of the mesoporous channel has no diffraction peaks,[8] the observed weak diffraction peaks are considered to be due to the guest that exists inside of the host channels. From the fwhm value of the Lorentzian profile which is similarly preserved within the error range as the pore diameter decreases, the estimated average particle diameters of 7.7−7.9 nm listed in Table 2 indicate that the particle size of the guest does not depend largely on the pore diameters of the host channels, and the particle shapes do not have the spherical morphology but rather have an elongated morphology along the one-dimensionally ordered host channels.[11] Furthermore, from the nitrogen adsorption data, the lateral dimension of the guest chalcogenide confined in the mesopores is suggested to be shorter than the diameter of the respective host channels.

Photoluminescence (PL) and Photoluminescence Excitation (PLE) Spectra. Figure 6 shows the PL and PLE spectra of the guest and a series of the nanocomposites at room temperature. The PL spectrum for the amorphous bulk of the ternary chalcogenide peaked around 450 nm (Figure 6a) shows broad and largely Stokes shifted feature compared with those of the nanocomposites (Figure 6b−d). Such a large Stokes shift is the characteristics of amorphous bulk materials. It is generally due to the small polarons generated in amorphous local structure of which the excited states have a strong tendency to lower their energies by deforming the surrounding network.[11,24,25] However, the PL spectrum for the NSTC16AlM is newly emerged around 330 nm (Figure 6b). Also, the spectrum is more narrowed and less Stokes shifted (0.63 eV) than that of the amorphous chalcogenide (Figure 6a). It implies that the structurally confined guest in the mesoporous channel forms a nanophase structure with increased crystallinity.[11]

For a series of the nanocomposites, the PL and the PLE spectra show a gradual shift to longer wavelengths (Figure 6b−d). The PL spectra of the NSTC16AlM, the NSTC14AlM, and the NSTC12AlM appear at about 330, 350, and 410 nm, respectively, which are Stokes shifted (0.5−0.9 eV) from the corresponding PLE spectra. Furthermore, the PL spectra of the nanocomposites exhibit the fwhm values of 0.75, 0.75, and 0.77 eV, respectively. These broad PL spectra are believed to be due to the various emission centers, such as possible defect sites, existing in the nanocomposites. Chestnoy suggested that the broad PL spectra of semiconductor particles occurred because of the distribution of the distant pairs of electron and hole centers which strongly coupled with the lattice phonon, especially longitudinal optical (LO) phonon.[26] Therefore, the observed PL spectra with the broad peak profile may occur because of the broad distribution of the distant pairs between the electron and the hole centers as well as the various defects.

The interesting point on the PLE spectra of a series of the nanocomposites is the peak splitting compared with the single PLE band of the amorphous bulk. The lowest energy bands of the nanocomposites are red shifted and peaked at 270, 300, and

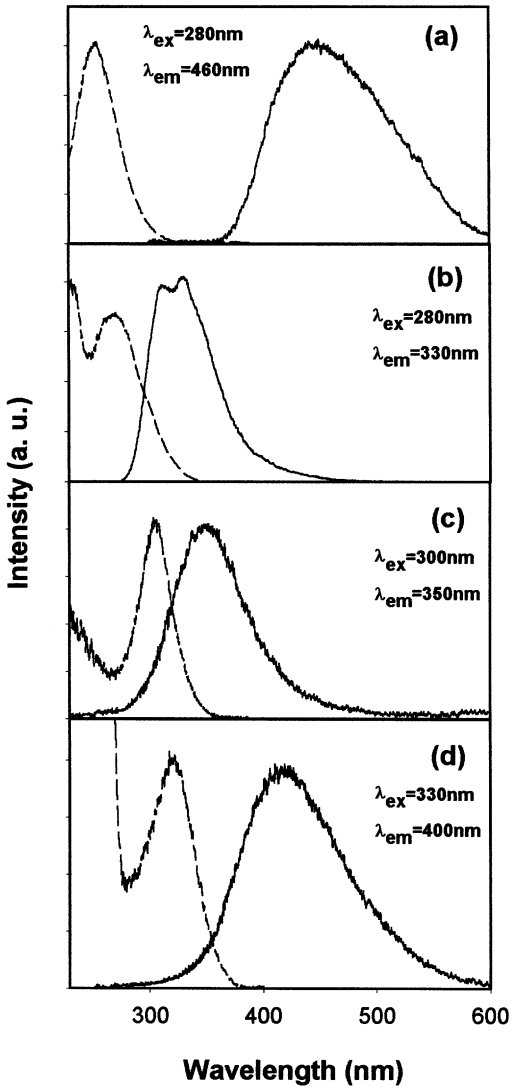

Figure 6. PL (solid line) and PLE (dashed line) spectra at room temperature: (a) amorphous $Ni_3(SbTe_3)_2$, (b) NSTC16AlM, (c) NSTC14AlM, and (d) NSTC12AlM. λ_{ex} and λ_{em} represent an excitation wavelength for PL spectrum and a detection wavelength for PLE spectrum, respectively. The PL and PLE spectra of the amorphous $Ni_3(SbTe_3)_2$ and NSTC16AlM are quoted from the previous study.[11]

310 nm with decreasing the pore diameter. It is noticeable that these lowest energy bands are located at the intermediate state between the PLE band (250 nm) and the small polaron energy state (PL band at 450 nm) of the amorphous bulk (Figure 6a).[11] As mentioned in the powder XRD analysis, the nanocomposites with the mesoporous host of smaller pore diameter appear to have larger fwhm values and amplitudes of the corresponding Gaussian components. Such characteristics implies that the guest is more affected, in respect of the lattice strain, by the static pressure from the host channel of smaller diameter. Therefore, it is considered that the observed lowest electronic absorption bands are originated from the indirect electronic transition involving the intermediate potential energy states which may occur because of the lattice strain of the guest induced by the static pressure from the mesoporous channel of large tube curvature.

Exciton−LO Phonon Coupling. Phonon coupling is a crucial factor on the performance of micro- and optoelectronics. Therefore, it is important to investigate the degree of phonon coupling to the excited carriers in the nanocomposites of the spin-glass material, $Ni_3(SbTe_3)_2$, incorporated in a series of the

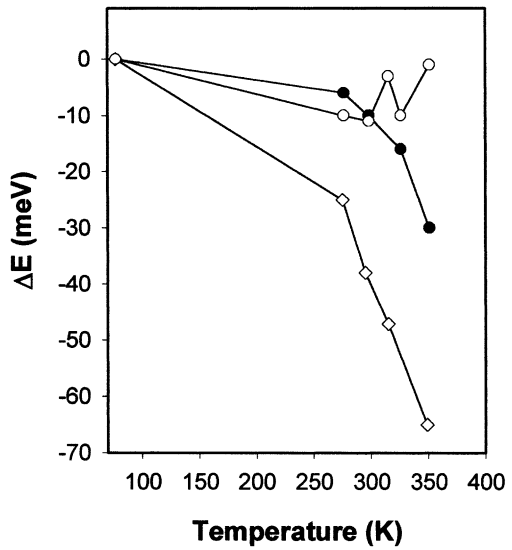

Figure 7. Temperature-dependent PL peak shift of NSTC16AlM (◇), NSTC14AlM (●), and NSTC12AlM (○) in the temperature range of 77−350 K. The temperature-dependent PL peak energies are presented as relative energy shift compared with the peak energies measured at 77 K for the respective nanocomposites.

host channels. Temperature dependence of the relative PL band shift is presented in Figure 7. As the host pore diameter decreases, the PL band energy shift becomes less sensitive to the temperature change. For the NSTC12AlM, the energy shift of the PL band is almost independent to the temperature. Although the exact evaluation of the phonon coupling in these nanocomposite materials is difficult to be done, it has been tried to estimate the relative tendency of phonon coupling to the photogenerated carriers that are deeply trapped in the localized states induced by the strong coupling of the guest and the host wall.

For the temperature dependence of the excitonic PL band energy, the phenomenological expression based on the Bose−Einstein model was proposed by Viña et al.[27,28] Because the longitudinal acoustic (LA) phonon coupling is negligible at a higher temperature above 77 K, the excited carrier relaxation mainly takes place via the LO phonon coupling (Fröhlich interaction) as the following expression:[29]

$$\Delta E(T) = -\alpha_0\left[\frac{1}{\exp(\Theta/T) - 1} + 1\right] \qquad (2)$$

where $\Delta E(T)$ is the temperature dependent change of the PL band energy, α_0 is the fitting parameter, and Θ is the effective phonon temperature expressed by $\hbar\omega_{LO}/k_B$. α_0 was determined from the relative band energy shift of the PL spectra of the respective nanocomposites at the temperature range of 77−350 K (Figure 7). For the least-squares fitting procedure, we used the effective phonon temperature of $\Theta = 86$ K which had been reported in the reference,[11] based on the approximation that the relative magnitude of the LO phonon interaction is not very sensitive to the LO phonon frequency in nanoscaled domain.[29] For the guests in the different pore diameters of the hosts, the α_0 is fitted to be 0.011 (± 0.002), 0.004 (± 0.001), and 0.002 (± 0.001) with decreasing the pore diameter, respectively. The estimated trend of the α_0 values shows a gradual decrease in the nanocomposites of the smaller pore diameter, which implies that the LO phonon coupling to the photogenerated carriers in the guest are reduced with decreasing the host pore diameter. In the nanoscaled systems, the exciton (electron−hole pair) Bohr radius is generally more compressed as the particle size

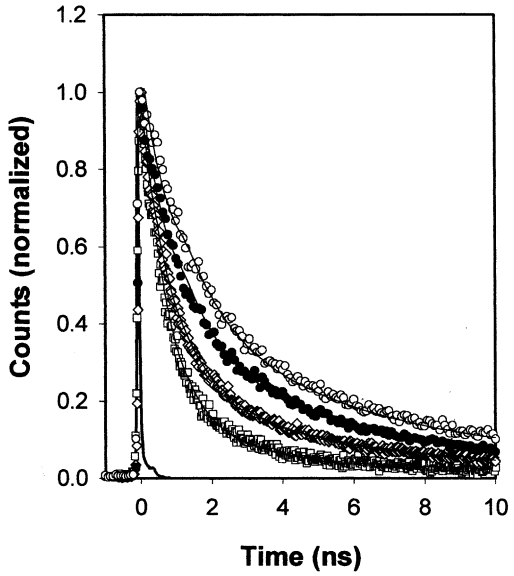

Figure 8. Time-resolved PL decays at room temperature: amorphous $Ni_3(SbTe_3)_2$ (□), NSTC16AlM (◇), NSTC14AlM (●), NSTC12AlM (○), and instrumental response function (IRF; thick solid line). Fitted lines are superimposed on the respective PL decays (thin solid line). The excitation wavelength is 287 nm. The detection wavelengths are 450, 330, 350, and 400 nm for the amorphous $Ni_3(SbTe_3)_2$, NSTC16AlM, NSTC14AlM, and NSTC12AlM, respectively. The PL decays for the amorphous $Ni_3(SbTe_3)_2$ and NSTC16AlM are quoted from the previous study.[11]

TABLE 3: Fluorescence Lifetimes of the Nanocomposites of Different Pore Diameters[a]

$Ni_3(SbTe_3)_2$ in hosts	λ_{em} (nm)	τ_1 (ns)	τ_2 (ns)	τ_3 (ns)	$\langle t \rangle$	χ^2
bulk $Ni_3(SbTe_3)_2$	450	0.1 (48.5%)	0.7 (42.9%)	3.7 (8.6%)	2.1	1.5
NSTC16AlM	330	0.2 (39.1%)	1.1 (45.7%)	6.5 (15.2%)	4.5	1.1
NSTC14AlM	350	0.7 (61.4%)	3.5 (30.6%)	13.9 (7.9%)	7.4	1.4
NSTC12AlM	400	0.8 (58.4%)	4.0 (33.3%)	17.0 (8.3%)	9.2	1.3

[a] $I(t) = A_1e^{-t/\tau_1} + A_2e^{-t/\tau_2} + A_3e^{-t/\tau_3} + ...$; $I(t)$ is the time-dependent PL intensity, A is the amplitude, and τ is the lifetime. The mean lifetimes are deduced as follows; $\langle\tau\rangle = \sum_i A_i\tau_i^2/\sum_i A_i\tau_i$. The excitation wavelength is 287 nm. λ_{em} represents the detection wavelength.

decreases. Thus, the exciton becomes less polar and the magnitude of its interaction with LO phonon is reduced in smaller nanodomain.[30] In these nanocomposites, however, the reduction of the nanodomain size is not so prominent with decreasing the diameter of the mesoporous channels, from the XRD analysis. Therefore, it is considered that the apparent reduction of the LO phonon coupling is possibly induced by the strong structural confinement of the guest in smaller mesoporous channel. Such suppression of the LO phonon coupling in the nanocomposites of smaller pore diameter is well consistent with the longer PL lifetimes in these systems, which is described in the following section.

Time-Resolved Photoluminescence Decays. The time-resolved PL decays in Figure 8 show the different lifetimes of the ternary chalcogenide incorporated in a series of the hosts of the different pore diameters. The PL decays are observed to consist of multiple lifetime components due to the complicated relaxation processes through the various defects existing in the nanocomposites[25] and/or the possible distant pairs distributions between the trapped electrons and holes.[26] Thus, the lifetimes are presented as the mean lifetimes as well as the fitted lifetimes (Table 3). The PL lifetimes observed for the series of the nanocomposites become longer with decreasing the host pore diameter (Figure 8). Although the PL spectrum of the

NSTC12AlM appears in the similar wavelength region with the PL spectrum for the bulk guest (Figure 6), the lifetimes are much different each other. Such a result suggests that the PL spectrum of the NSTC12AlM reveals the characteristics of the structurally confined ternary chalcogenide in the mesoporous channels of the C12AlMCM host.

For these nanocomposite materials, the observed PL lifetimes include information on the recombination processes of the trapped carriers in the deeply localized states (0.5−0.9 eV) of the nanophase chalcogenide. In these deeply localized trap states, it is believed that the photoexcited carrier recombination probably occurs mainly by the phonon coupling.[26,31] Therefore, the recombination probability of the trapped electrons in the localized states and the holes in the valence band increases as the phonon coupling increases. Such increased recombination probability results in the faster recombination lifetime. According to this carrier recombination process, the apparently reduced recombination rate of the nanocomposites in this study implies that the recombination process experiences less phonon coupling in the smaller host channel, which is consistent with the results from the temperature dependent PL experiment. Such prominent reduction of the LO phonon coupling to the photoexcited carriers in the structurally confined ternary chalcogenide can be probably induced from the static pressure by the inner wall framework of the mesoporous AlMCM-41 host. Therefore, the suppression of phonon coupling in the ternary chalcogenide nanocomposites becomes even stronger in smaller host channel, resulting the longer PL lifetime.

Conclusions

We incorporated the structurally, optically, and magnetically interesting amorphous ternary chalcogenide of $Ni_3(SbTe_3)_2$ into the channel of AlMCM-41 hosts. The TEM images present the incorporated nanocomposites of the ternary chalcogenide in a series of the hosts of the different pore diameters. It seems that the smaller channel size hinders the anionic Zintl precursors from the effective insertion into their inner channels during the rapid precipitation. As the amorphous guest is confined in 1-D channels, the guest structure is arranged in the inside of the mesoporous channels to give a long range ordered pattern. For the ternary chalcogenide in smaller host channel diameter, the degree of the lattice strain is enlarged, whereas the particle size is similar. The incorporation of the guest into the host channel is also efficiently characterized by the PL and PLE spectra that show the red shift of the lowest electronic transition band, which is due to the structural confinement of the guest by the host channel. The reduction of the phonon coupling to the photoexcited carriers in the guest nanodomain is possibly ascribed to the enhanced static pressure induced by the structural confinement in the mesoporous channel, which results the longer recombination lifetime with decreasing the mesopore diameter.

Acknowledgment. This work was financially supported by a grant (No. 1999-2-121-004-5) from Korea Science and Engineering Foundation. We are grateful for the instrumental support from the equipment facility of CRM-KOSEF, Korea University.

References and Notes

(1) O'Connor, C. J.; Jung, J.-S.; Zhang, J. H. In *Chemistry, Structure, and Bonding of Zintl Phases and Ions*; Kauzlarich, S. M., Ed.; VCH Publisher: New York, 1996; Chapter 7.

(2) Haushalter, R. C.; O'Connor, C. J.; Umarji, A. M.; Shenoy, G. K.; Saw, C. K. *Solid State Commun*. **1984**, *49*, 929.

(3) Haushalter, R. C.; O'Connor, C. J.; Haushalter, J. P.; Umarji, A. M.; Shenoy, G. K. *Angew. Chem*. **1984**, *96*, 147.

(4) Haushalter, R. C.; O'Connor, C. J.; Haushalter, J. P.; Umarji, A. M.; Shenoy, G. K. *Angew. Chem., Int. Ed. Engl*. **1984**, *23*, 169.

(5) Foise, J. W.; Haushalter, F. C.; O'Connor, C. J. *Solid State Commun.* **1987**, *63*, 349.

(6) Zhang, J. H.; vanDuyneveldt, A. J.; Mydosh, J. A.; O'Connor, C. J. *Chem. Mater*. **1989**, *1*, 404.

(7) Zhang, J. H.; Wu, B.; O'Connor, C. J. *Chem. Mater*. **1993**, *5*, 17.

(8) Jung, J.-S.; Ren, L.; O'Connor, C. J. *J. Mater. Chem*. **1992**, *2*, 829.

(9) Jung, J.-S.; Wu, B.; Ren, L.; Tang, J.; Ferre, J.; Jamet, J.; O'Connor, C. J. *J. Mater. Res*. **1994**, *9*, 909.

(10) Jung, J.-S.; Stevens, E. D.; O'Connor, C. J. *J. Solid State Chem*. **1991**, *94*, 362.

(11) Chae, W.-S.; Hwang, I.-W.; Jung, J.-S.; Kim, Y.-R. *Chem. Phys. Lett.* **2001**, *341*, 279.

(12) Kresge, C. T.; Leonowicz, M. E.; Roth, W. J.; Vartuli, J. C.; Beck, J. S. *Nature*, **1992**, *359*, 710.

(13) Jung, J.-S.; Chae, W.-S.; McIntyre, R. A.; Seip, C. T.; Wiley, J. B.; O'Connor, C. J. *Mater. Res. Bull*. **1999**, *34*, 1353.

(14) Kim, J. M.; Kwak, J. H.; Jun, S.; Ryoo, R. *J. Phys. Chem*. **1995**, *99*, 16742.

(15) Fenelonov, V. B.; Romannikov, V. N.; Derevyankin, A. Yu. *Micropor. Mesopor. Mater*. **1999**, *28*, 57.

(16) Kruk, M.; Jaroniec, M.; Sakamoto, Y.; Terasaki, O.; Ryoo, R.; Ko, C. H. *J. Phys. Chem. B* **2000**, *104*, 292.

(17) Parala, H.; Winkler, H.; Kolbe, M.; Wohlfart, A.; Fischer, R. A.; Schmechel, R.; Seggern, H. *Adv. Mater*. **2000**, *12*, 1050.

(18) Brieler, F. J.; Fröba, M.; Chen, L.; Klar, P. J.; Heimbrodt, W.; Nidda, H.-A. K.; Loidl, A. *Chem. Eur. J*. **2002**, *8*, 185.

(19) Kruk, M.; Jaroniec, M.; Sayari, A. *J. Phys. Chem. B* **1997**, *101*, 583.

(20) Kruk, M.; Jaroniec, M.; Sayari, A. *Langmuir* **1997**, *13*, 6267.

(21) Kruk, M.; Jaroniec, M.; Sayari, A. *Chem. Mater*. **1999**, *11*, 492.

(22) Klug, H. P.; Alexander, L. E. *X-ray Diffraction Properties for Polycrystalline and Amorphous Materials*; Wiley: New York, 1974.

(23) Chen, W.; Xu, Y.; Lin, Z.; Wang, Z.; Lin, L. *Solid State Commun*. **1998**, *105*, 129.

(24) Anderson, P. W. *Nature (London) Phys. Sci*. **1972**, *235*, 163.

(25) Brodsky, M. H. *Amorphous Semiconductors*; Springer-Verlag: New York, 1979.

(26) Chestnoy, N.; Harris, T. D.; Hull, R.; Brus, L. E. *J. Phys. Chem*. **1986**, *90*, 3393.

(27) Viña, L.; Logothetidis, S.; Cardona, M. *Phys. Rev. B* **1984**, *30*, 1979.

(28) Logothetidis, S.; Viña, L.; Cardona, M. *Phys. Rev. B* **1985**, *31*, 947.

(29) Ramvall, P.; Tanaka, S.; Nomura, S.; Riblet, P.; Aoyagi, Y. *Appl. Phys. Lett*. **1999**, *75*, 1935.

(30) Alivisatos, A. P.; Harris, T. D.; Carroll, P. J.; Steigerwald, M. L.; Brus, L. E. *J. Chem. Phys*. **1989**, *90*, 3463.

(31) O'Neil, M.; Marohn, J.; McLendon, G. *J. Phys. Chem*. **1990**, *94*, 4356.